Article

Not peer-reviewed version

Top of the Atmosphere Reflected Shortwave Radiative Fluxes from ABI on GOES-18

Yingtao Ma , Rachel T. Pinker * , Wen Chen , Istvan Laszlo , Hye-Yun Kim , Hongqing Liu , Jaime Daniels

Posted Date: 4 July 2025

doi: 10.20944/preprints202507.0386.v1

Keywords: GOES-R ABI; shortwave radiative fluxes; top of the atmosphere radiative fluxes; narrow to broadband transformations

Article

Top of the Atmosphere Reflected Shortwave Radiative Fluxes from ABI on GOES-18

Yingtao Ma [1,2], Rachel T. Pinker [1,*], Wen. Chen [1], Istvan Laszlo [3], Hye-Yun Kim [4], Hongqing Liu [4] and Jaime Daniels [3]

1 Department of Atmospheric and Oceanic Science, University of Maryland, College Park, MD, USA
2 Cooperative Institute for Research in the Atmosphere (CIRA), Colorado State University, CO, USA
3 NOAA NESDIS Center for Satellite Applications and Research, College Park, MD, USA
4 I.M. Systems Group, Inc., Rockville, MD, USA
* Correspondence: pinker@umd.edu

Abstract

In this study we describe the derivation and evaluation of Top of the Atmosphere (TOA) Shortwave Radiative (SWR) Fluxes from the Advanced Baseline Imager (ABI) sensor on the GOES-18 satellite. The TOA estimates use narrow-band observations from ABI that are transformed to broadband (NTB), based on simulations and adjusted to total fluxes using Angular Distribution Models (ADM). Subsequently, the GOES-18 estimates are evaluated against the Clouds and the Earth's Radiant Energy System (CERES) data, the only available source of information over the GOES-18 domain. The importance of agreement at the TOA is because most methodologies to derive surface SWR start with the satellite observation at the TOA. Moreover, information on radiative fluxes at both boundaries (TOA and surface) is needed for estimating the energy absorbed by the atmosphere. The methodology described has been comprehensively evaluated and possible sources of errors were identified. The results of the evaluation for the four seasonal months indicate that by using the best available auxiliary data the accuracy achieved in estimating TOA SWR at instantaneous scale ranges between 0.55 to 17.14 W m^{-2} for the bias and 22.21 to 31.20 W m^{-2} for the standard deviation of biases (differences are ABI minus CERES). It is believed that the high bias of 17.14 for July is related to the predominantly cloudless sky conditions when the used ADMs do not perform as well as for cloudy conditions.

Keywords: GOES-R ABI; shortwave radiative fluxes; top of the atmosphere radiative fluxes; narrow to broadband transformations

---

1. Introduction

Our climate is controlled by the surface energy budget on a global scale and is dominated by radiative fluxes. The incoming shortwave radiation (SWR) from the sun that reaches the Earth's surface is a dominant component of this budget. Strides in technical capabilities of satellites make them a primary source for information at large scales. Satellites, originally polar orbiters, have become an integral part of most programs to monitor climate. The limitation and impact of poor representation of the diurnal cycle from polar orbiters has been recognized and interest in geostationary satellites has increased. Yet, satellite-based estimates differ from each other and from those provided by numerical models. Major differences are related to quality of satellite observations, such as the frequent changes in satellite observing systems, degradation of sensors, restricted spectral intervals, viewing geometry of sensors, and changes in the quality of atmospheric inputs that drive the inference schemes. Achievable accuracy is also related to the lack of maturity of basic information needed in the implementation process, such as a reliable cloud screened product which is in a process of development and modifications (Loeb et al. 2005). Reducing differences among the satellite-based estimates requires, among others, updates to inference schemes so that the most recent auxiliary information can be fully utilized.

Two products, the reflected SWR at top of atmosphere and the downward SWR at surface are routinely generated at NOAA from the Advanced Baseline Imager (ABI) onboard the GOES-R series of US satellites (Laszlo et al. [1], Laszlo et al. [2]). Both products require a shortwave broadband top-of-atmosphere (TOA) albedo converted from six ABI narrowband reflectance (Table 1). Critical elements of an inference scheme for TOA radiative flux estimates from satellite observations are: 1) transformation of narrowband quantities into broadband ones; 2) transformation of bi-directional reflectance into albedo by applying Angular Distribution Models (ADMs). The narrow-to-broadband (NTB) conversion used in this study is derived from simulated broadband and narrowband reflectance as detailed in Pinker et al. [3] for the ABI on GOES-16 and 17. Observation-based broadband ADMs derived primarily from the Clouds and the Earth's Radiant Energy System (CERES) are used to complete the derivation of the TOA radiative flux. The "ground truth", namely, the CERES observations are also undergoing adjustments and recalibration. As such, an evolutionary process can be expected as demonstrated in this study by emphasizing changes made in our approach when dealing with GOES-18 as compared to GOES-16 and 17. New spectral characteristics of ABI onboard GOES-18 have been applied to the simulated narrowband fluxes. The procedure of matching GOES-18 observations with those from CERES have been updated. We used the radiance from the ABI product, converted it to reflectance, applied NTB conversions and ADMs before comparing to CERES fluxes. We used the radiances in six relevant ABI bands (out of sixteen) as shown in Table 1.

Table 1. Wavelength, type and resolution of the six ABI bands used in this study.

ABI Band	Central wavelength (μm)	type	Best spatial resolution
1	0.47	Visible	1
2	0.64	Visible	0.5
3	0.86	Near-IR	1
4	1.37	Mear-IR	2
5	1.6	Near-IR	1
6	2.2	Near-IR	2

Each band has a different resolution. Before use we resampled them to 2 km. Subsequently, these 2 km data were remapped to the 20 km CERES data. Previously, we remapped the CERES observations to those of GOES-16 and 17. Now we remap the high-resolution observations from GOES-18 to those of CERES. In Section 2 we describe the entire process that includes a brief description of methodology, data used, matching of observations between ABI/GOES-18 and CERES Single Scanner Footprint (SSF) and averaging the ABI data to match the CERES pixel; in section 3 we present results and in section 4 we discuss and summarize the findings.

2. Approach

2.1. Methodology

We briefly describe the physical basis and the development of the NTB transformations of satellite observed radiances and the bi-directional corrections to be applied to the broadband reflectance to obtain broadband TOA albedo. A detailed description as applies to GOES-16 and 17 can be found in Pinker et al. [3]. The Advanced Baseline Imager (ABI) observations onboard of the NOAA GOES-R series of satellites provide reflectance in six narrow bands in the shortwave spectrum**.** The following is done: 1) calculation of TOA high-resolution spectral and broadband (total shortwave) reflectance with MODTRAN-4.3 (Berk et al. [4]) and scene dependent land use classifications from the International Geosphere-Biosphere Programme (IGBP) (Hansen et al. [5]); 2) convolution of the high-resolution spectral reflectance to simulate ABI narrowband reflectance; 3) regression of the simulated ABI reflectance against the broadband reflectance calculated in step 1. The ADMs from CERES (Loeb et al., [6]) were augmented with theoretical simulations (Niu and Pinker, [7]). This was done to extend the observational CERES database that was under sampled in certain directions (angular bins). Surface conditions were one of the primary inputs into the MODTRAN simulations. The International Geosphere-Biosphere Programme (IGBP) land classification (Hansen et al., [5]; Loveland et al., [8]) dataset is at 1/6° resolution and includes 18 surface types. We have converted the 1/6° (~18.5 km) resolution to the ABI 2-km grid using the nearest grid method. The method for cloudy sky uses four surface types; these are also derived from 12 IGBP types (Pinker et al. [3]). Modifications to these procedures when applied to GOES-18 will be described in sections 2.3 and 2.4.

2.2. Data Used

L1B GOES-18 radiance data files for the CONUS domain (file names OR_ABI-L1b-RadC-) were downloaded from the NOAA Comprehensive Large Array-Data Stewardship System (https://www.aev.class.noaa.gov/) and the ABI Spectral Response Function (SRF) from NOAA's Center for Satellite Application and Research Calibration Center website (https://ncc.nesdis.noaa.gov/GOESR/ABI.php. Not all the required angular information needed for implementation of regressions was available online and had to be recomputed (such as solar geometry). Reference data for CERES observation were downloaded from (https://cmr.earthdata.nasa.gov/search/concepts/C7460991-LARC_ASDC.html. Data file name is "CERES_SSF_Terra-XTRK_Edition4A_Subset".

2.3. Matching Observations Between ABI/GOES-18 and CERES SSF

ABI on GOES-18 is a geostationary sensor at nadir longitude of 137° W. The Pacific U.S. (PACUS) sector coverage of the GOES-West satellite is 12° N-60° N, 90° W-175° W, as shown in Figure 1. (For details: https://www.star.nesdis.noaa.gov/goes/index.php.)

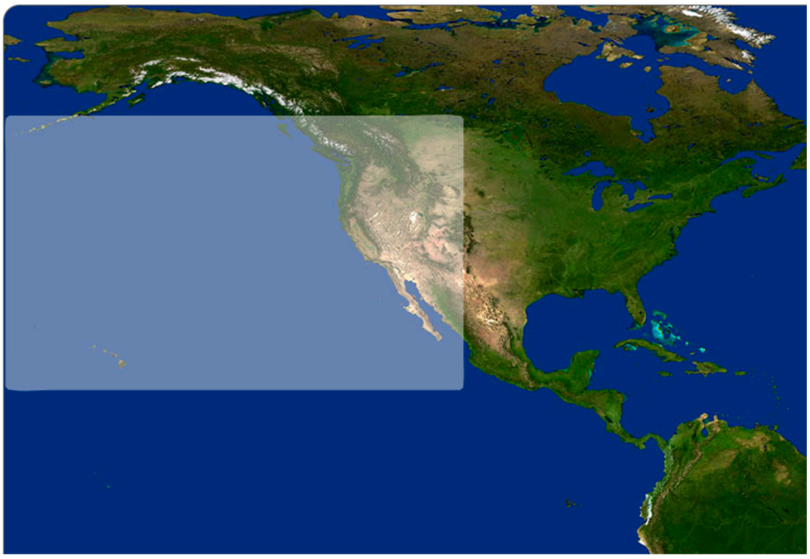

Figure 1. Illustration of the Pacific U.S. (PACUS) sector coverage of the GOES-West (currently, GOES-18) satellite.

The ABI GOES-18 data are provided as images for each observation time on a fixed grid whose coordinate values are the sensor scanning angle in units of radians relative to the satellite sub-point location. The fixed grid is rectified to an ellipsoid defined by the Geodetic Reference System 1980 (GRS80) earth model. The navigation between the fixed grid coordinates (scanning angle in east/west and elevation angle in north/south) and geodetic latitude and longitude is determined by the geostationary satellite projection or fixed grid projection (FGP). Details can be found in "GOES R

Preprints.org (www.preprints.org) | NOT PEER-REVIEWED | Posted: 4 July 2025 doi:10.20944/preprints202507.0386.v1

SERIES PRODUCT DEFINITION AND USERS' GUIDE" (https://www.goes-r.gov/users/docs/PUG-main-vol1.pdf).

Below (Figure 2) is an example of matchup between CERES and ABI for day 327 in 2022, 21:21:17 UTC.

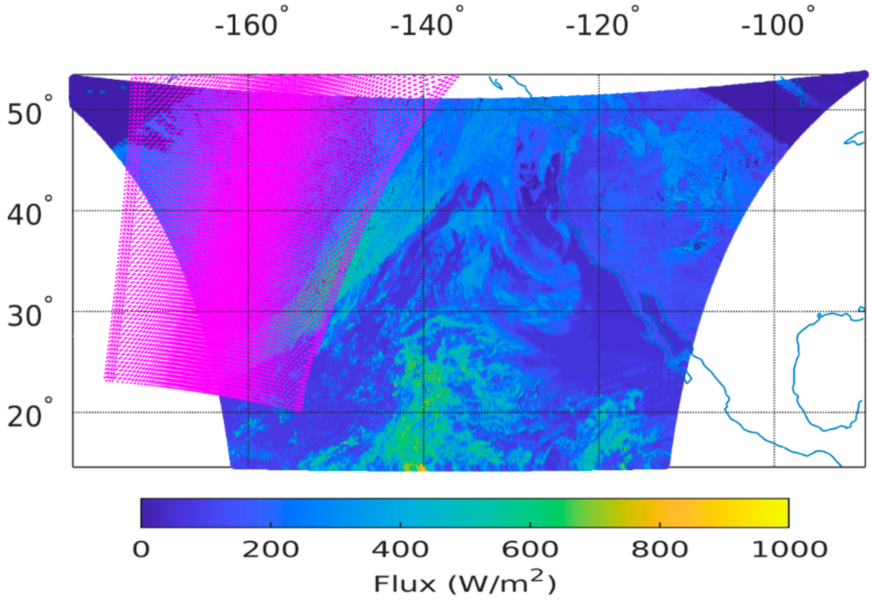

Figure 2. An example of matchup between CERES and ABI for day 327 in 2022, 21:21:17 UTC. The blue background is the ABI TOA radiative flux, and the magenta indicates the CERES pixels that overlap with the ABI.

The CERES data are given in a time series format. Every CERES pixel's longitude, latitude and time are provided along with the flux data. To find the matchups, we loop over each ABI image time and search in the CERES time series to find the CERES pixels that fall in the ABI domain within a certain period. For example, given an ABI image timed at 2022-12-1 17:15:00 with area coverage from 15º N to 50º N latitude and from 170º W to 80º W longitude, we find that there are 502 CERES pixels that fall within the area in a time interval of +/-5 minutes around the ABI time as shown in Figure 3a.

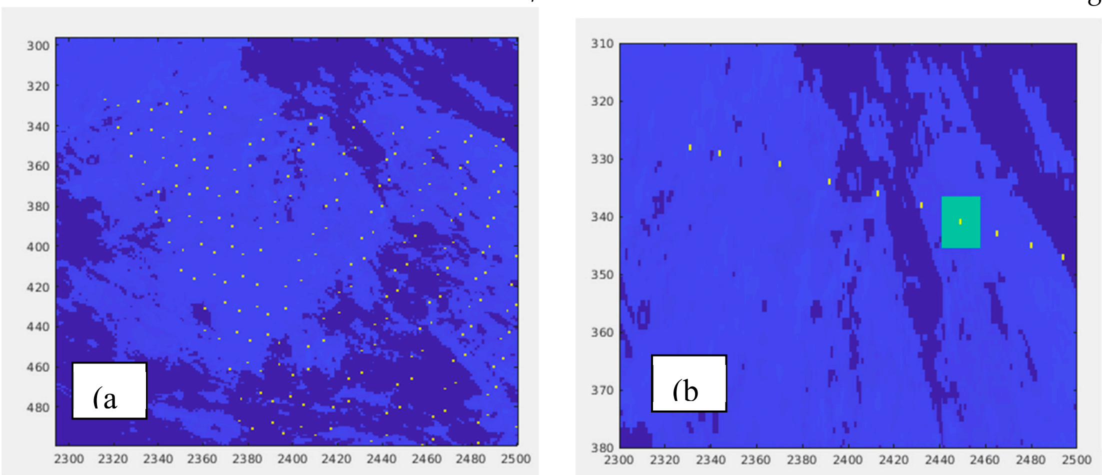

Figure 3. (a): An example of finding CERES pixels that fall within the ABI domain around 2022 12 1, 17:15:00 UTC. x, y axis are ABI CONUS image column and row number (out of 1500 x 2500). Each point represents the center of a single CERES SSF footprint. **(b)**: Average of ABI data to match the CERES SSF data. Panel (b) is for the same time as that for (a). The small white rectangles show the center location of 10 CERES pixels. The green block is a 16x32 km block of ABI data centered on a CERES pixel.

Preprints.org (www.preprints.org) | NOT PEER-REVIEWED | Posted: 4 July 2025 doi:10.20944/preprints202507.0386.v1

We illustrate with a case for November 2022. We use CERES Single Scanner Footprint (SSF) data (Terra and Aqua) from November 23 to December 1, 2022. The number of overlapping pixels ranges from 0 to 18,000 for Terra and 16,000 for Aqua. From all ABI images available from November 23 thirty-eight cases for Terra to December 1, 2022, the number of images that overlap with CERES data are counted and shown in Table 2.

Table 2. Number of available ABI images with pixels overlapping with CERES data within the time period from November 23 to December 1, 2022.

# of overlap pixels	CERES/Terra	CERES/Aqua
>500	128	78
>1000	121	72
>5000	87	43
>10000	47	21
>12000	36	16
>15000	13	7

If we chose only those ABI images with more than 12,000 overlap pixels, for CERES/Aqua, we have sixteen matchups between CERES and ABI at a specific (single) ABI time as listed in Appendix A. Next, we process these ABI cases to obtain TOA fluxes and do the comparison with the co-located CERES data.

2.4. Averaging ABI Data to Match the CERES Pixel.

Due to the fixed grid projection format (FGF) used to store the ABI data, one can easily transform the map coordinates between the longitude/latitude format and ABI image col/row format. This analytic way to calculate the location of the matchup pixel in ABI image saves time compared to searching through the whole ABI image to find the location of the matchups.

ABI flux data have 2-km nadir resolution. CERES Field of View (FOV) is about 16x32 km (the 20 km is a nominal spatial resolution that is roughly the same size as 16*32 km). When matching ABI with CERES, we first calculate the col/row location of the CERES pixel in the ABI image. Around that location, a 16x32 km block of ABI data is extracted and averaged to match the CERES SSF data (this is the values at nadir, however, in this study we use the same size for all CERES FOVs). An example is shown in Figure 3b.

Since ABI data are available about every 5 minutes for the CONUS domain, there might be more than one ABI image that overlaps with a CERES pixel within the 10-minute time interval. In such a situation, the ABI data from all available times within the 10-minute time interval and within the 16x32 block are averaged to match the CERES data.

2.5. Experiments with New ADMs

For GOES-16 and 17 used were ADMs as described in Loeb et al. [6]. The next-generation ADMs that were developed for Terra and Aqua using all available CERES rotating azimuth plane radiance measurements (Su et al. [9]) are not yet available to the public and therefore, not used in this study. CERES radiance measurements are stratified by scene type and by other parameters that are important for determining the anisotropy of the given scene. As reported in Su et al. [10], significant differences between the new and the older ADMs are for clear-sky scene and polar scene types. Over clear land, the ADMs are developed for every 1° latitude × 1° longitude region for every calendar month. It is claimed that compared to the Loeb at al. [6] ADMs (hereafter CERES2003 ADM), the new ADMs change the monthly mean instantaneous fluxes by up to 5 W m^{-2} on a regional scale of 1° latitude × 1° longitude, but the flux changes are less than 0.5 W m^{-2} on a global scale.

 doi:10.20944/preprints202507.0386.v1

Match ups between ABI and CERES SSF TOA fluxes in 2022-11-23 00Z to 2022-12-01 23Z have been used. There were twenty-one cases for Aqua and forty-seven cases for Terra (Appendix A).

As seen in Figure 4, compared to the CERES TOA fluxes, the ABI fluxes are larger in the low range (CERES TOA fluxes less than about 100 W m^{-2}) and smaller in the high range (CERES TOA fluxes larger than about 250 W m^{-2}). The low and high ranges generally correspond to cloud-free scenes (and or low solar zenith angles) and cloudy (and or high solar zenith angles), respectively. In the mid-range (approximately between 100 and 250 W m^{-2}), there is a large scatter of data points, several of them with significant negative ABI-CERES TOA flux differences. However, most of them are clustered around the one-to-one line. As a result, the frequency distribution of the ABI-CERES TOA flux differences peaks around zero with a large negative tail. Another peak at about a positive 30 W m^{-2} is present that comes from the low range of CERES fluxes as shown in the density scatterplot. We have conducted several experiments to identify the reason for this secondary peak.

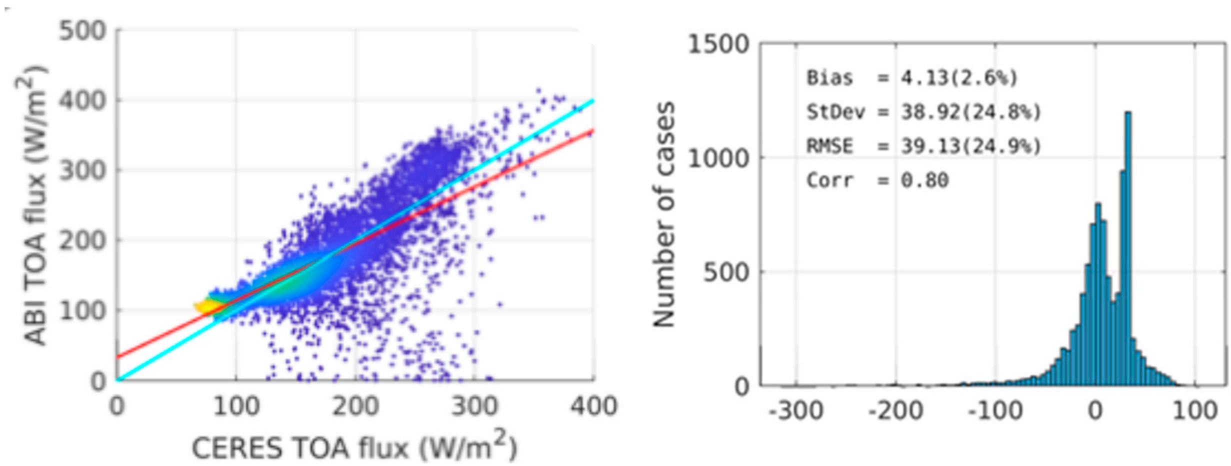

Figure 4. Results for a single granule for year 2022 day 329 at 17:46 UTC using the CERES2003 ADM. Density scatterplot of ABI vs. CERES TOA fluxes (left), and histogram of ABI-CERES differences (right). In the density scatter plot, the solid red line is the linear fit line, and the light blue line is the one-to-one line.

2.5.1. Experiment 1

We applied the old approach (Pinker et al. [3]) to the ADMs and the secondary spike disappeared. The old approach is based on a synergy between the original CERES ADMs as described in Loeb et al. [6] and simulations, as described in Niu and Pinker [7]. The bias increased but there was some reduction in the standard deviation of biases.

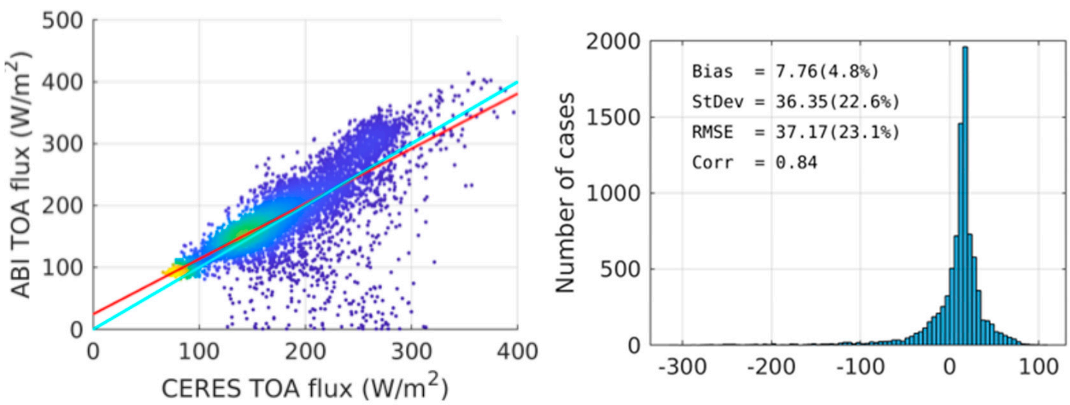

Figure 5. Same granule as used in Figure 4, but using the older ADM approach.

2.5.2. Experiment 2

 doi:10.20944/preprints202507.0386.v1

In the second experiement we have used the CERES2003 ADM for all surface types except for clear ocean. For clear ocean we replaced it with our original ADMs that combined the CERES2003 ADM models and our simulations (Niu and Pinker [7]) (hereafter Niu2011 ADM). This resulted in lower ABI fluxes in the mid range, which in turn increased the number of points below the one-to-one line and reduced the overall bias, but with practically no change in the standard deviation. (Figure 6).

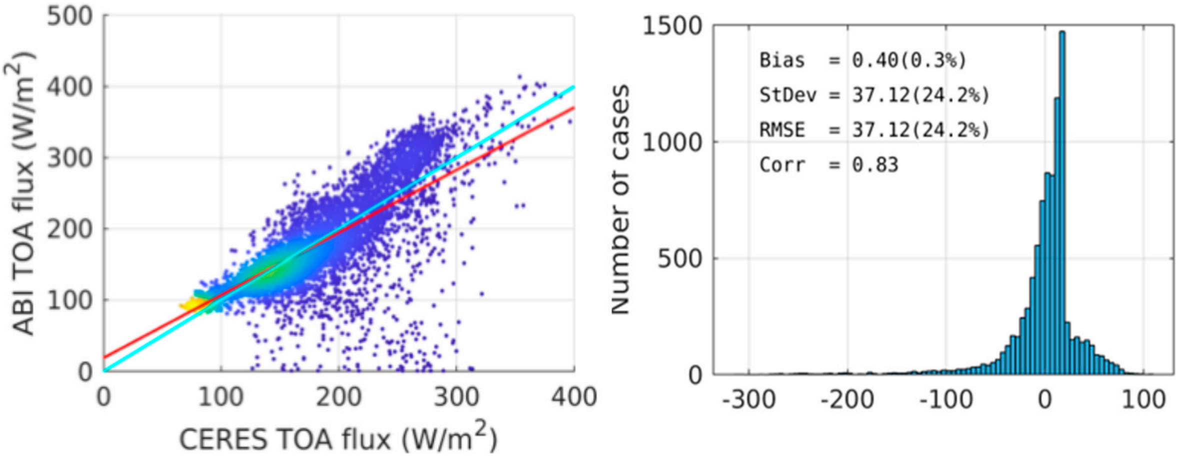

Figure 6. Here we use CERES2003 ADMs except for the clear ocean where ADM values are replaced with the old, combined ADMs (Niu2011 ADM); same cases as used previously.

2.5.3. Experiment 3

Based on the improvement seen in Experiment 2, we have redone all the cases for November 2022 using this approach (for clear ocean). The cases used are detailed in *Appendix A.* A summary of the results are shown in Figure 7 and detailed in *Appendix B*. As evident, substantial improvement has been achieved.

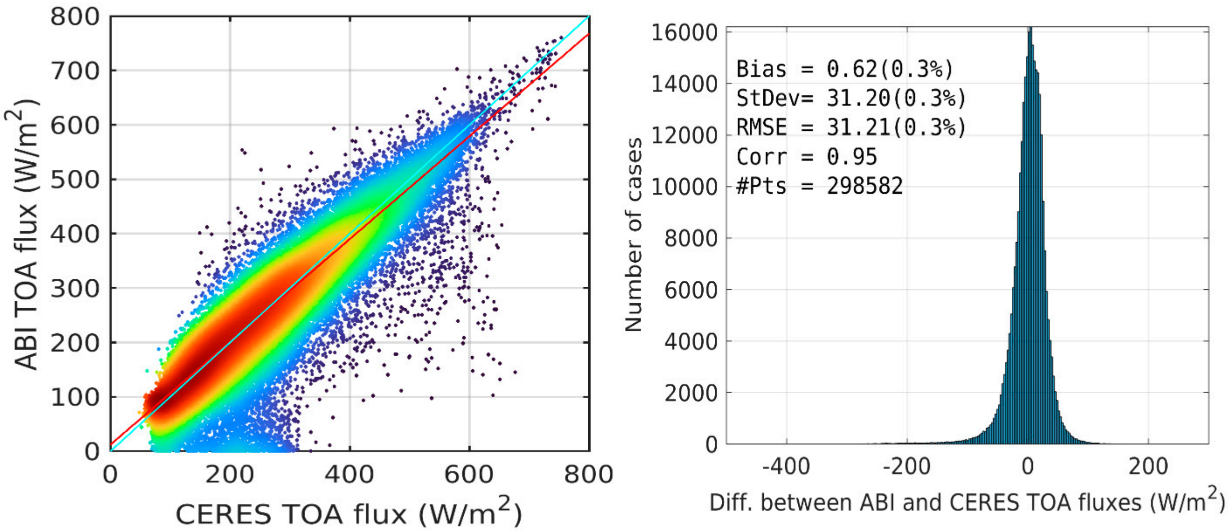

Figure 7. These results are for November 2022 using all the cases listed in *Appendix A.* The ADM used is CERES2003 ADMs except for the ocean where ADM values are replaced with the old, synthesized ADMs.

3. Results

3.1. Results for January, April, and July After Removing Outliers

Outliers are defined as data points with std greater than three. At least for some of the outliers, the large differences are from locations where there are only a few valid pixels available in the

 doi:10.20944/preprints202507.0386.v1

corresponding CERES box. In this case, the block average may not be representative of the real condition of the CERES box. The scatter plots after removing the outliers are shown below. The ADM used is the CERES2003 ADMs with ocean ADM values replaced with the old, synthesized ADMs.

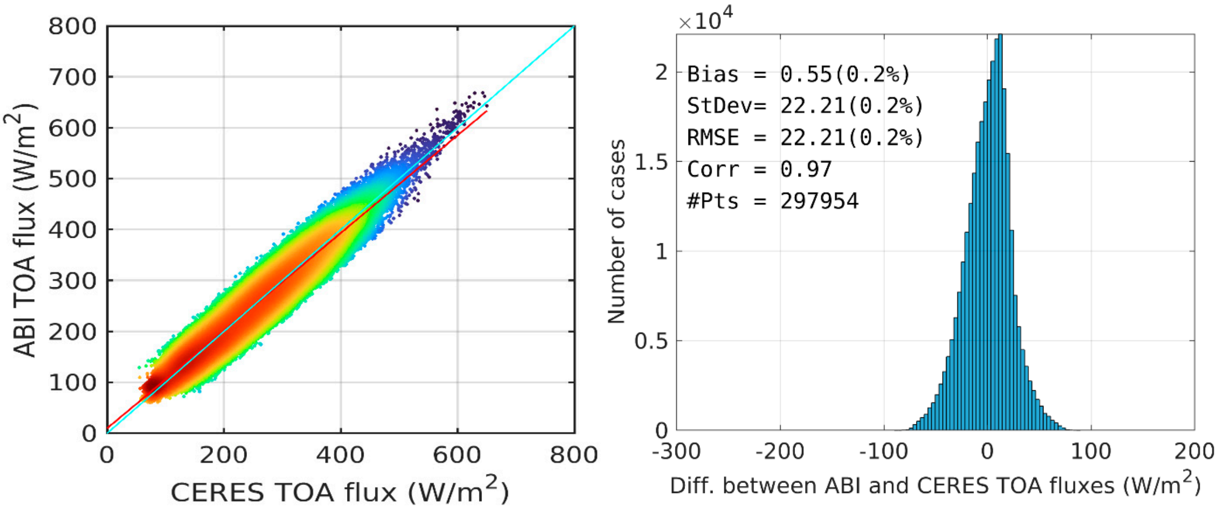

Figure 8. ABI TOA flux compared to CERES TOA flux for January 2023. The number of outliers removed was 0.7 %.

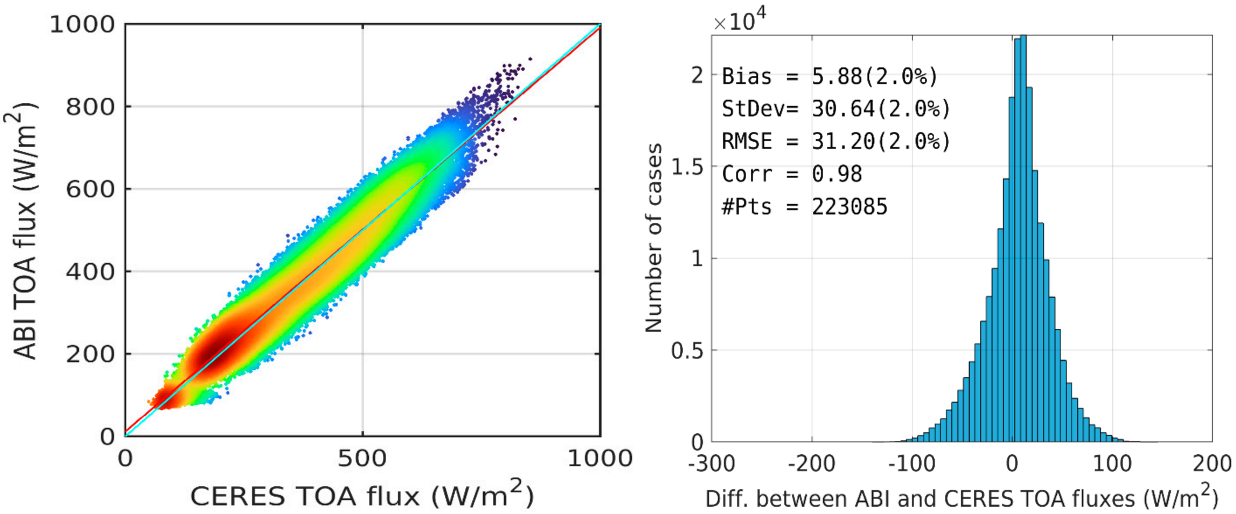

Figure 9. ABI TOA flux compared to CERES TOA flux for April 2023. The number of outliers removed was 1 %.

Preprints.org (www.preprints.org) | NOT PEER-REVIEWED | Posted: 4 July 2025 doi:10.20944/preprints202507.0386.v1

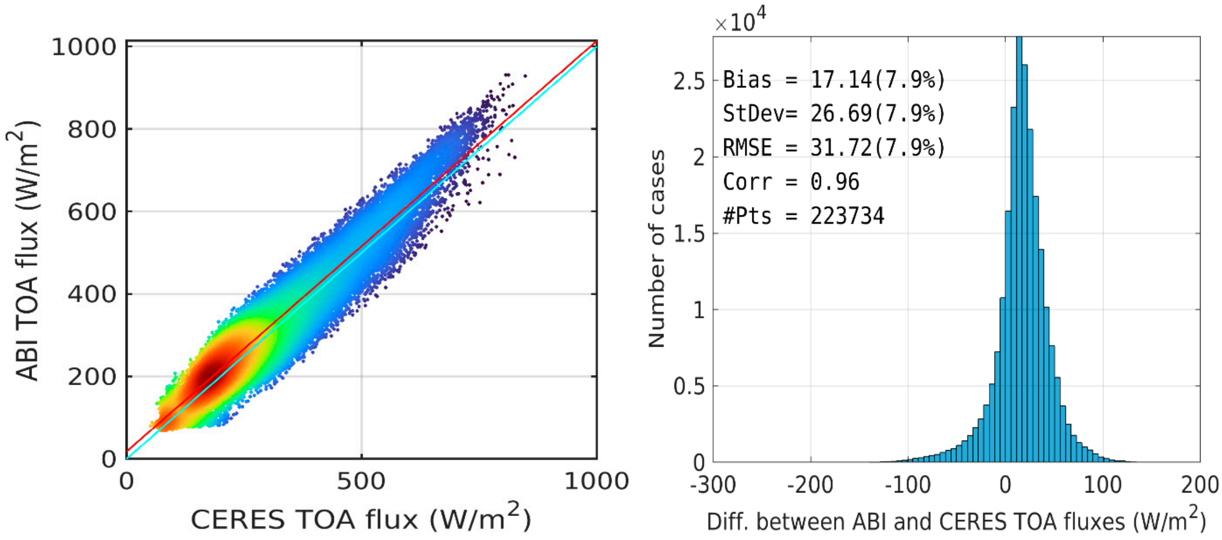

Figure 10. ABI TOA flux compared to CERES TOA flux for July 2023. The number of outliers removed was 2 %.

3.2. Investigation of the July Case

To better understand why the results for July agree less with CERES than those for the other three months, we have investigated the cloudy conditions during the selected months. For example, we have plotted the conditions for each day for July and April 2023. We illustrate each month with one case. The notations in the following figures are:

(a) Matchup between ABI and CERES swaths. Red pixels are CERES FOVs.

(b) ABI flux image in 2-km resolution matched to CERES swath.

(c) ABI flux image re-gridded to CERES resolution. Matched to CERES swath.

(d) CERES flux image.

(e) Density scatter plot between CERES and ABI.

(f) Histogram and statistics.

(g) ABI cloud fraction.

(h) ABI 640-nm cloud optical depth.

In the following figure we illustrate the cloud conditions for 14th of July 2023. The figures show TOA fluxes that are considered as proxy for the presence of clouds Illustrated are also the results of evaluation as specified above for (a) to (f). (g) and (h) show the ABI cloud fraction and the 640-nm cloud optical depth, respectively.

Preprints.org (www.preprints.org) | NOT PEER-REVIEWED | Posted: 4 July 2025 doi:10.20944/preprints202507.0386.v1

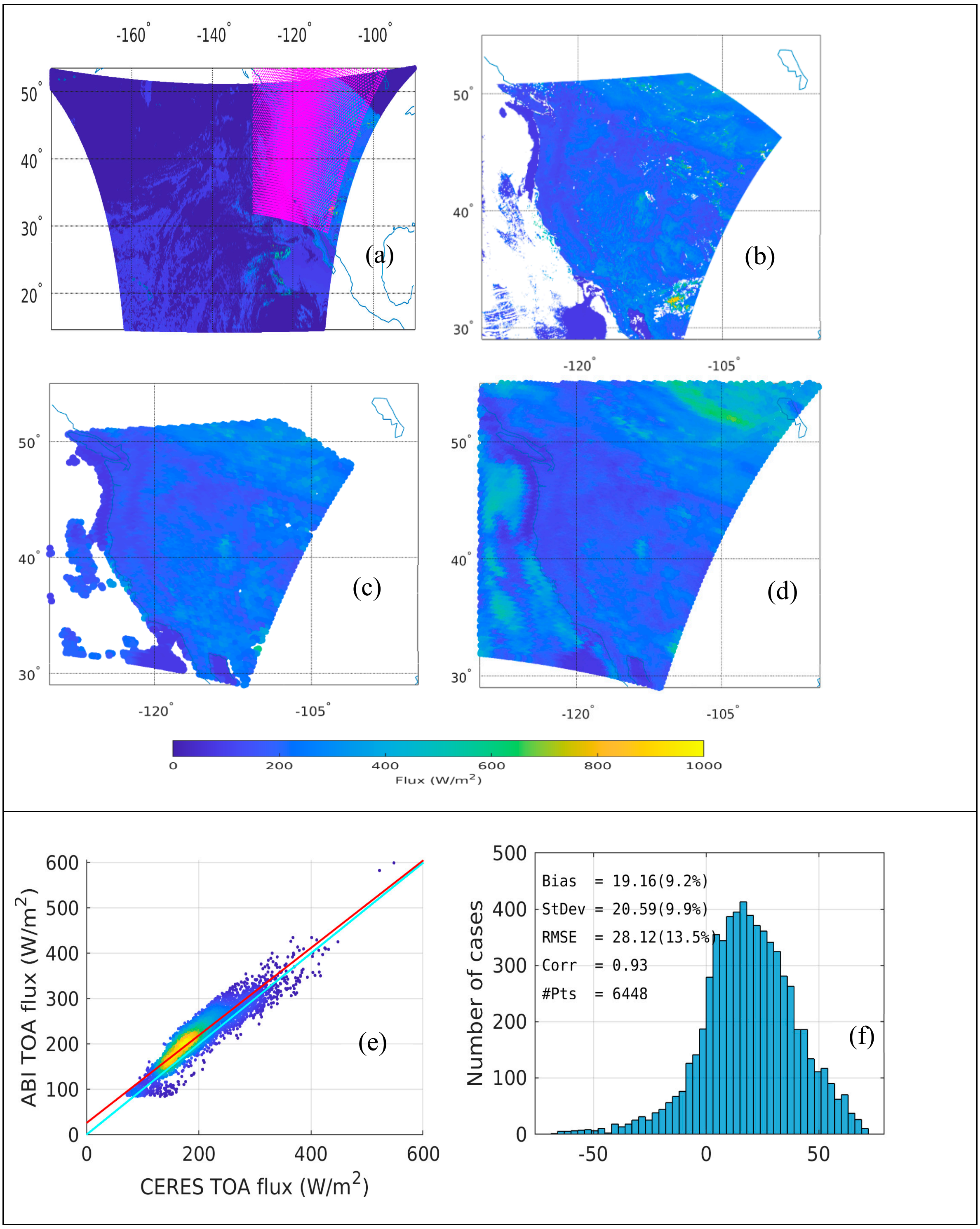

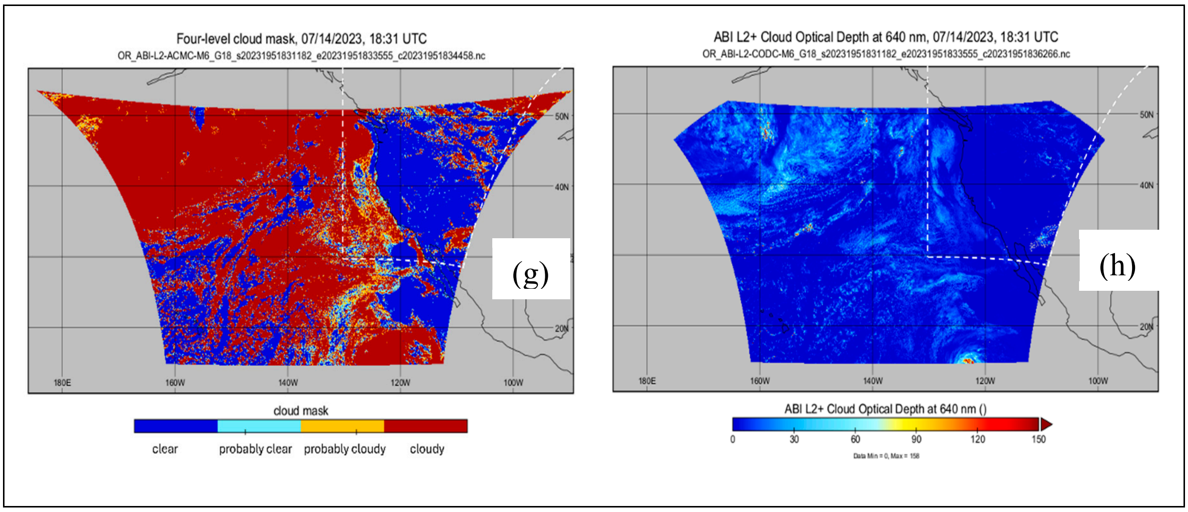

Figure 11. The cloud conditions during 14th of July 2023, 18:31:18 UTC and relevant results of evaluation. (a) Matchup between ABI and CERES swaths. Red pixels are CERES FOVs. (b) 2-km ABI flux matched to the CERES swath. (c) ABI flux matched to the CERES swath and re-gridded to CERES resolution. (d) CERES flux. (e) Density scatter plot between CERES and ABI. (f) Histogram and statistics. (g) ABI cloud fraction. (h) ABI 640-nm cloud optical depth. The region within the white dashed lines in (g) and (h) marks the approximate area of CERES observations.

It was established, and shown in Fig. 11 specifically for July 14, 2023, that most July cases have clear conditions or thin clouds over the ABI-CERES overlap region. The higher bias comes mainly from the clear pixels.

We have also investigated cloud conditions during April 2023. In April, cloudy cases are more frequent than in July. A case for April is shown in Figure 12. We see a lower bias in April than in July.

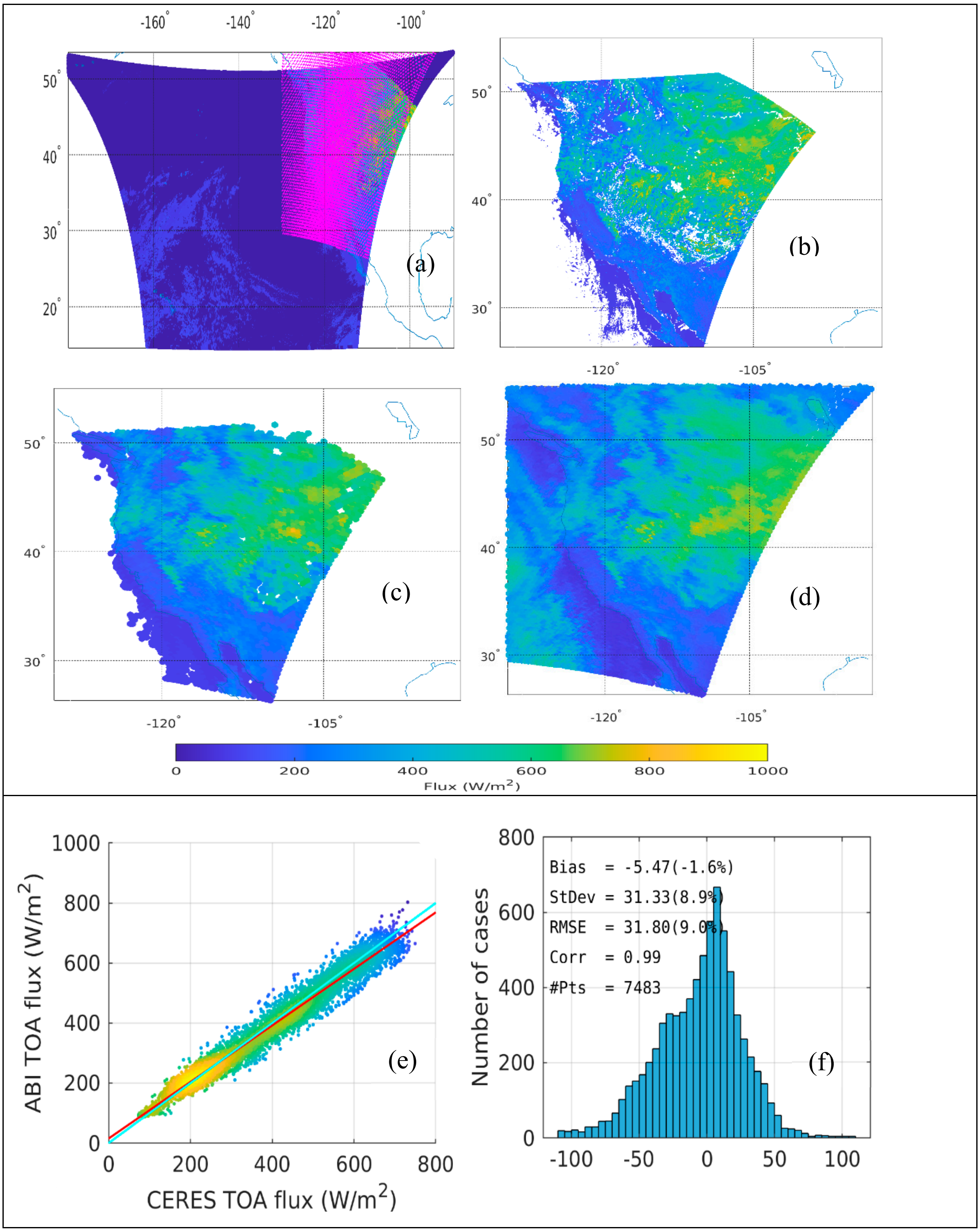
(a)
(b)
(c)
(d)
Flux (W/m2)
(e)
ABI TOA flux (W/m2)
CERES TOA flux (W/m2)
(f)
Number of cases
Bias = -5.47(-1.6%)
StDev = 31.33(8.9%)
RMSE = 31.80(9.0%)
Corr = 0.99
#Pts = 7483

Preprints.org (www.preprints.org) | NOT PEER-REVIEWED | Posted: 4 July 2025 doi:10.20944/preprints202507.0386.v1

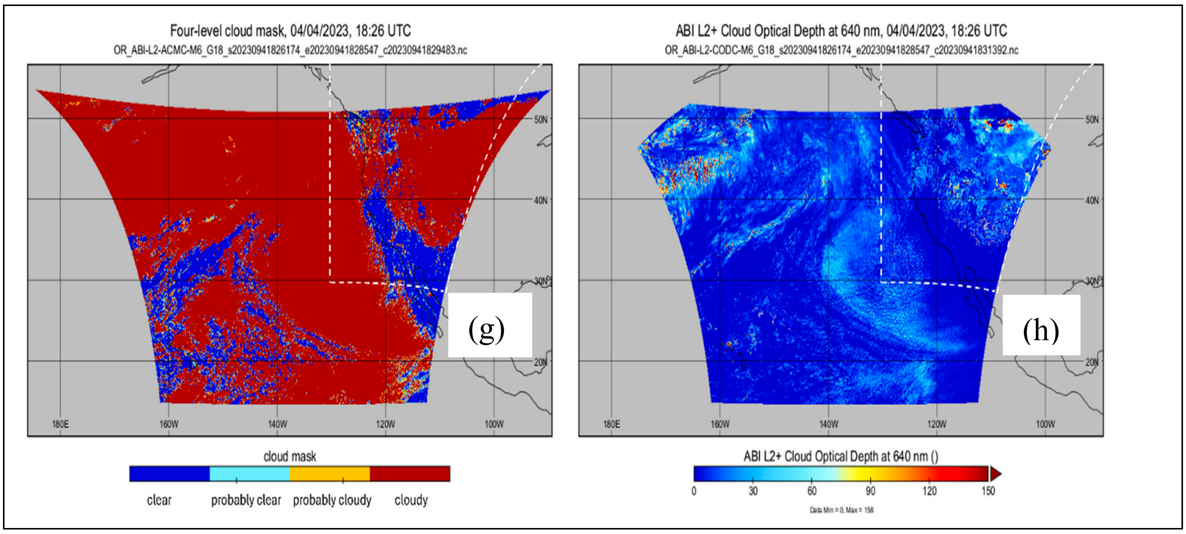

Figure 12. Same as Figure 11 but for April 4, 2023, 18:26:17 UTC.

4. Discussion and Summary

Most satellite observations provide information at TOA only and observe in narrow spectral bands. To derive the total flux at the TOA as well as at the surface there is a need to transform such observations into broadband fluxes. This is accomplished primarily by simulations that require validation against broadband observations. The primary source of broadband observations at the TOA comes from CERES; however, these observations also require some empirical corrections using Angular Distribution Models (ADM). As such, there is no absolute "truth" available for evaluations. In this study we use narrow-band observations from ABI on GOES-18 that are transformed to broadband based on simulations (NTB) and adjusted to total fluxes using an ADM that is a combination of the CERES2003 ADM and the Niu2011 ADM for ocean to estimate the broadband flux. Subsequently, the GOES-18 estimates are evaluated against the Clouds and the Earth's Radiant Energy System (CERES) data, the only available source of such information. The importance of agreement at the TOA is because most methodologies to derive surface SWR fluxes start with the satellite observation at the TOA. Moreover, information on radiative fluxes at both boundaries (TOA and surface) is needed for estimating the energy absorbed by the atmosphere. The methodology described to make such comparisons has been evaluated and possible sources of error were identified.

We have completed an evaluation of shortwave (SW) radiative fluxes at the top of the atmosphere (TOA) as derived from GOES-18 against CERES for four months during 2022 representing different seasons. This is the first effort to evaluate ABI for GOES-18 for such an extensive time period. In contrast to evaluation of GOES-16 and 17, we have remapped ABI observations to CERES. Previously, the mapping was from CERES to ABI. Previous experiments have shown that mapping procedures do have an impact on the results. The results of the evaluation indicate that the accuracy achieved in estimating TOA SWR fluxes ranges between 0.55 to 17.14 for the bias and 22.21 to 31.20 for the std. It is believed that the high bias of 17.14 for July is related to the predominantly clear sky conditions when the used ADMs may have some problems.

Author Contributions: The investigation and conceptualization were carried out by RTP, IL and JD. YM and WC developed the software. RTP prepared the original draft. All authors contributed to the writing, editing and review of the publication.

Competing interests: The authors declare that they have no conflict of interest.

Acknowledgments: We acknowledge the benefit from the use of the numerous data sources used in this study. These include the Clouds and the Earth's Radiant Energy System (CERES) teams, the Fast Longwave and Shortwave Radiative Flux (FLASHFlux) teams, the University of Wisconsin-Madison, Space Science and

 doi:10.20944/preprints202507.0386.v1

Engineering Center, Cooperative Institute for Meteorological Satellite Studies (CIMSS) for providing the SeeBor Version 5.0 data (https://cimss.ssec.wisc.edu/training_data/, and the final versions of the GOES Imager data were downloaded from https://www.bou.class.noaa.gov/. Several individuals have been involved in the early stages of the project whose contribution led to the refinement of the methodologies. These include M. M. Woncsick and Shuyan Liu.

Financial support: This research was supported by NOAA/STAR GOES-R Program under CISESS grant NA19NES4320002, award numbers RPRP_DASR_23 and RPRP_DASR_24 to the University of Maryland.

Appendix A

The list below is the GOES images that overlap with CERES Aqua and Terra satellite in November 2022. Every one of these GOES images has >10000 CERES SSFs within the GOES domain.

Match ups between ABI and CERES SSF data in 2022-11-23 00Z to 2022-12-01 23Z.

For Aqua:

```
OR_ABI-L1b-RadC-M6C06_G18_s20223272006173_e20223272008552_c20223272008583.nc
OR_ABI-L1b-RadC-M6C06_G18_s20223272011173_e20223272013552_c20223272013586.nc
OR_ABI-L1b-RadC-M6C06_G18_s20223272146173_e20223272148552_c20223272148582.nc
OR_ABI-L1b-RadC-M6C06_G18_s20223272151173_e20223272153552_c20223272153585.nc
OR_ABI-L1b-RadC-M6C06_G18_s20223282051175_e20223282053553_c20223282053582.nc
OR_ABI-L1b-RadC-M6C06_G18_s20223291956176_e20223291958555_c20223291958581.nc
OR_ABI-L1b-RadC-M6C06_G18_s20223292131176_e20223292133555_c20223292133582.nc
OR_ABI-L1b-RadC-M6C06_G18_s20223292136176_e20223292138555_c20223292138586.nc
OR_ABI-L1b-RadC-M6C06_G18_s20223302036177_e20223302038557_c20223302038587.nc
OR_ABI-L1b-RadC-M6C06_G18_s20223302041177_e20223302043556_c20223302043588.nc
OR_ABI-L1b-RadC-M6C06_G18_s20223311941179_e20223311943558_c20223311943588.nc
OR_ABI-L1b-RadC-M6C06_G18_s20223312121179_e20223312123558_c20223312123597.nc
OR_ABI-L1b-RadC-M6C06_G18_s20223322021170_e20223322023549_c20223322023584.nc
OR_ABI-L1b-RadC-M6C06_G18_s20223322026170_e20223322028549_c20223322028580.nc
OR_ABI-L1b-RadC-M6C06_G18_s20223332106172_e20223332108550_c20223332108584.nc
OR_ABI-L1b-RadC-M6C06_G18_s20223332111172_e20223332113550_c20223332113584.nc
OR_ABI-L1b-RadC-M6C06_G18_s20223342011173_e20223342013552_c20223342013580.nc
OR_ABI-L1b-RadC-M6C06_G18_s20223342016173_e20223342018552_c20223342018579.nc
OR_ABI-L1b-RadC-M6C06_G18_s20223342151173_e20223342153552_c20223342153580.nc
OR_ABI-L1b-RadC-M6C06_G18_s20223352051175_e20223352053553_c20223352053580.nc
OR_ABI-L1b-RadC-M6C06_G18_s20223352056175_e20223352058553_c20223352058589.nc
```

For Terra:

```
OR_ABI-L1b-RadC-M6C06_G18_s20223271801173_e20223271803552_c20223271803580.nc
OR_ABI-L1b-RadC-M6C06_G18_s20223271806173_e20223271808551_c20223271808582.nc
OR_ABI-L1b-RadC-M6C06_G18_s20223271941173_e20223271943552_c20223271943579.nc
OR_ABI-L1b-RadC-M6C06_G18_s20223271946173_e20223271948552_c20223271948584.nc
OR_ABI-L1b-RadC-M6C06_G18_s20223272121173_e20223272123552_c20223272123582.nc
OR_ABI-L1b-RadC-M6C06_G18_s20223281706174_e20223281708553_c20223281708583.nc
```

 doi:10.20944/preprints202507.0386.v1

OR_ABI-L1b-RadC-M6C06_G18_s20223281841174_e20223281843553_c20223281843585.nc

OR_ABI-L1b-RadC-M6C06_G18_s20223281846174_e20223281848553_c20223281848583.nc

OR_ABI-L1b-RadC-M6C06_G18_s20223282021174_e20223282023553_c20223282023582.nc

OR_ABI-L1b-RadC-M6C06_G18_s20223282026174_e20223282028553_c20223282028584.nc

OR_ABI-L1b-RadC-M6C06_G18_s20223291746176_e20223291748554_c20223291748590.nc

OR_ABI-L1b-RadC-M6C06_G18_s20223291751176_e20223291753554_c20223291753582.nc

OR_ABI-L1b-RadC-M6C06_G18_s20223291926176_e20223291928555_c20223291928589.nc

OR_ABI-L1b-RadC-M6C06_G18_s20223292101176_e20223292103555_c20223292103582.nc

OR_ABI-L1b-RadC-M6C06_G18_s20223292106176_e20223292108555_c20223292108587.nc

OR_ABI-L1b-RadC-M6C06_G18_s20223301651177_e20223301653556_c20223301653585.nc

OR_ABI-L1b-RadC-M6C06_G18_s20223301826177_e20223301828556_c20223301828588.nc

OR_ABI-L1b-RadC-M6C06_G18_s20223301831177_e20223301833556_c20223301833589.nc

OR_ABI-L1b-RadC-M6C06_G18_s20223302006177_e20223302008556_c20223302008589.nc

OR_ABI-L1b-RadC-M6C06_G18_s20223302011177_e20223302013556_c20223302013584.nc

OR_ABI-L1b-RadC-M6C06_G18_s20223302146178_e20223302148556_c20223302148587.nc

OR_ABI-L1b-RadC-M6C06_G18_s20223311731179_e20223311733557_c20223311733589.nc

OR_ABI-L1b-RadC-M6C06_G18_s20223311736179_e20223311738557_c20223311738584.nc

OR_ABI-L1b-RadC-M6C06_G18_s20223311911179_e20223311913558_c20223311913585.nc

OR_ABI-L1b-RadC-M6C06_G18_s20223312046179_e20223312048558_c20223312048589.nc

OR_ABI-L1b-RadC-M6C06_G18_s20223312051179_e20223312053558_c20223312053589.nc

OR_ABI-L1b-RadC-M6C06_G18_s20223321811170_e20223321813549_c20223321813577.nc

OR_ABI-L1b-RadC-M6C06_G18_s20223321816170_e20223321818549_c20223321818578.nc

OR_ABI-L1b-RadC-M6C06_G18_s20223321951170_e20223321953549_c20223321953577.nc

OR_ABI-L1b-RadC-M6C06_G18_s20223321956170_e20223321958549_c20223321958577.nc

OR_ABI-L1b-RadC-M6C06_G18_s20223322131170_e20223322133549_c20223322133579.nc

OR_ABI-L1b-RadC-M6C06_G18_s20223331716171_e20223331718550_c20223331718578.nc

OR_ABI-L1b-RadC-M6C06_G18_s20223331851171_e20223331853550_c20223331853583.nc

OR_ABI-L1b-RadC-M6C06_G18_s20223331856171_e20223331858550_c20223331858583.nc

OR_ABI-L1b-RadC-M6C06_G18_s20223332031172_e20223332033550_c20223332033577.nc

OR_ABI-L1b-RadC-M6C06_G18_s20223332036172_e20223332038550_c20223332038587.nc

OR_ABI-L1b-RadC-M6C06_G18_s20223341756173_e20223341758552_c20223341758585.nc

OR_ABI-L1b-RadC-M6C06_G18_s20223341801173_e20223341803552_c20223341803580.nc

OR_ABI-L1b-RadC-M6C06_G18_s20223341936173_e20223341938552_c20223341938579.nc

OR_ABI-L1b-RadC-M6C06_G18_s20223342111173_e20223342113552_c20223342113582.nc

OR_ABI-L1b-RadC-M6C06_G18_s20223342116173_e20223342118552_c20223342118581.nc

OR_ABI-L1b-RadC-M6C06_G18_s20223351701174_e20223351703553_c20223351703586.nc

OR_ABI-L1b-RadC-M6C06_G18_s20223351836174_e20223351838553_c20223351838580.nc

OR_ABI-L1b-RadC-M6C06_G18_s20223351841175_e20223351843554_c20223351843586.nc

OR_ABI-L1b-RadC-M6C06_G18_s20223352016175_e20223352018554_c20223352018580.nc

OR_ABI-L1b-RadC-M6C06_G18_s20223352021175_e20223352023554_c20223352023584.nc

OR_ABI-L1b-RadC-M6C06_G18_s20223352156175_e20223352158553_c20223352158580.nc

doi:10.20944/preprints202507.0386.v1

Appendix B

Results for cases shown in Figure 7. Used is the CERES2003 ADMs except for the ocean where ADM values were replaced with the Niu2011 ADMs with number of overlapped pixels >10000. Included are the bias, standard deviation of the biases (stdev), the root mean squared error (rmserr), the percent bias (pbias), the percent standard deviation (pstd), and the correlation coefficient (corr).

bias	stdev	rmserr	pbias*	pstdev	corr
-0.85606	29.969	29.98	-0.47907	16.771	0.93384
-2.7	28.702	28.828	-1.1086	11.784	0.97182
2.181	34.005	34.073	1.0254	15.987	0.942
-12.429	39.888	41.768	-7.9541	25.526	0.76836
3.0505	28.044	28.208	1.8294	16.818	0.93876
-4.3455	34.155	34.429	-1.7507	13.76	0.95735
0.39935	37.114	37.114	0.26057	24.216	0.83205
-0.66335	29.371	29.377	-0.29131	12.898	0.96571
-0.34199	28.171	28.172	-0.13378	11.02	0.91855
-14.145	52.485	54.31	-8.8922	32.995	0.69622
6.9834	25.857	26.782	3.9258	14.536	0.95696
0.27233	28.699	28.699	0.11357	11.969	0.96866
10.119	34.905	36.34	5.0421	17.392	0.89984
-2.2489	34.614	34.684	-1.3104	20.169	0.90046
1.6483	24.734	24.788	0.76011	11.406	0.96314
5.9568	29.953	30.538	3.3553	16.871	0.92963
-3.7305	27.587	27.837	-1.7622	13.031	0.9513
5.1825	23.878	24.433	2.6886	12.388	0.96647
9.045	39.824	40.836	4.0588	17.871	0.90796
-9.4123	35.568	36.786	-4.8907	18.482	0.90337
-0.37148	25.745	25.747	-0.17625	12.215	0.95077
3.0198	31.089	31.234	1.4889	15.328	0.94944
-5.6674	30.726	31.243	-2.7831	15.089	0.93517
-7.7931	37.391	38.194	-3.6139	17.34	0.94338
10.44	27.521	29.433	4.9336	13.005	0.91576
-12.203	50.156	51.598	-7.1384	29.34	0.68105
0.89041	33.323	33.333	0.38101	14.259	0.94934
0.68753	24.821	24.83	0.34867	12.588	0.97111
-8.6732	41.674	42.564	-3.0728	14.764	0.877
-0.8863	32.7576	33.3159	-0.5223	16.5455	0.9119

 doi:10.20944/preprints202507.0386.v1

*pbias is % bias

Appendix C

Detailed Statistics for each matched case for January, April and July 2023.

Table C1. January, before removing outliers.

bias	stdev	rmserr	pbias	pstdev	prmserr	corr	numData
13.104	29.747	32.494	5.3286	12.097	13.214	0.94696	1180
0.45773	25.309	25.312	0.21162	11.701	11.702	0.97217	8985
-2.5804	20.551	20.711	-1.1447	9.1168	9.1878	0.97769	7144
-4.1269	23.16	23.524	-1.759	9.8712	10.026	0.96675	10551
-5.2965	23.058	23.655	-2.774	12.076	12.389	0.95631	4329
2.6288	24.095	24.237	1.1277	10.336	10.397	0.97184	10821
-2.1375	24.945	25.03	-1.0851	12.663	12.706	0.94767	2098
-1.3178	25.055	25.089	-0.5938	11.29	11.305	0.96471	9238
-0.66777	23.447	23.455	-0.3612	12.683	12.687	0.95339	9461
4.6342	22.732	23.199	2.1959	10.772	10.993	0.97086	11502
4.0747	24.06	24.401	1.937	11.438	11.599	0.96973	5364
1.689	23.421	23.481	0.75099	10.414	10.44	0.97376	12566
3.2493	23.902	24.118	1.5377	11.312	11.414	0.96506	3170
6.1204	25.909	26.62	2.5249	10.688	10.982	0.97358	8994
1.7406	24.585	24.645	0.89419	12.63	12.661	0.94372	8858
12.101	23.417	26.35	5.6804	10.992	12.369	0.95341	1183
6.3615	22.22	23.112	2.9713	10.378	10.795	0.97387	11787
10.007	24.525	26.487	4.2734	10.473	11.311	0.96856	14155
12.29	27.712	30.282	5.1862	11.694	12.778	0.91189	385
-0.032878	23.466	23.465	-0.012176	8.6902	8.6898	0.9728	10250
5.564	24.483	25.104	1.8739	8.2457	8.4549	0.9623	3968
0.6974	19.425	19.436	0.30349	8.4531	8.4582	0.98226	10953
-0.47176	23.426	23.426	-0.19619	9.7419	9.7417	0.9675	2241
-0.69884	25.326	25.334	-0.32141	11.648	11.652	0.96292	11247
-4.4586	23.092	23.518	-2.0541	10.639	10.835	0.96674	9932
7.7451	26.655	27.743	3.376	11.619	12.093	0.95598	866
-1.74	24.196	24.257	-0.84576	11.761	11.791	0.97138	11245
-6.7573	18.636	19.821	-3.325	9.1698	9.7532	0.97581	5812
0.32497	19.679	19.681	0.15	9.0839	9.0848	0.98479	12741
-2.1467	23.768	23.861	-0.87605	9.6994	9.7376	0.96599	3622
-2.6019	21.027	21.186	-1.242	10.037	10.113	0.97631	9266
-0.099278	22.266	22.26	-0.042418	9.5136	9.511	0.9634	1760
7.7764	19.779	21.251	3.9528	10.054	10.802	0.98055	8305

1.3074	22.653	22.69	0.55848	9.6771	9.6926	0.97328	8123
1.8388	21.974	22.049	0.81621	9.7535	9.7871	0.98052	10360
-0.21369	26.299	26.298	-0.082323	10.131	10.131	0.96942	5477
-10.653	24.022	26.277	-4.473	10.087	11.033	0.97197	11298
-7.7988	26.764	27.872	-3.061	10.505	10.94	0.94241	2586
-0.24185	27.161	27.16	-0.12118	13.609	13.609	0.96506	8660
-5.387	24.828	25.405	-2.2953	10.579	10.824	0.97326	10582

Table C2. January, after removing outliers.

bias	stdev	rmserr	pbias	pstdev	prmserr	corr	numData
11.614	27.119	29.491	4.7702	11.139	12.113	0.95504	1159
0.76158	22.324	22.336	0.35456	10.393	10.399	0.97802	8854
-2.9547	19.014	19.241	-1.3158	8.4674	8.5685	0.98087	7077
-3.4773	21.203	21.486	-1.4842	9.0504	9.1708	0.97204	10421
-5.2156	21.151	21.783	-2.7439	11.128	11.46	0.96269	4286
2.6296	22.926	23.075	1.1291	9.8444	9.9085	0.9745	10756
-2.3914	23.76	23.875	-1.2182	12.103	12.161	0.95195	2081
-0.90303	23.804	23.82	-0.4068	10.723	10.73	0.96848	9178
-0.74913	21.536	21.548	-0.40716	11.705	11.711	0.96045	9361
4.7698	21.13	21.661	2.2645	10.032	10.284	0.97508	11374
3.477	21.6	21.876	1.6658	10.348	10.48	0.97498	5283
1.4145	21.74	21.785	0.63085	9.6959	9.716	0.97737	12432
2.5599	22.453	22.595	1.2143	10.651	10.718	0.96942	3141
5.9148	25.238	25.92	2.4428	10.423	10.705	0.97518	8958
2.2825	22.469	22.583	1.1774	11.59	11.649	0.95127	8761
11.707	22.918	25.727	5.5106	10.788	12.11	0.95513	1176
5.8713	21.156	21.955	2.7488	9.9047	10.279	0.97648	11675
9.1296	22.549	24.327	3.9203	9.6827	10.446	0.97337	13932
11.645	26.827	29.213	4.9244	11.345	12.354	0.91793	382
-0.30366	22.34	22.341	-0.11266	8.2882	8.2885	0.97525	10165
5.1824	22.686	23.268	1.7469	7.6473	7.8433	0.96777	3925
0.93588	17.959	17.983	0.408	7.8294	7.8397	0.98486	10836
-0.60629	21.886	21.89	-0.2522	9.1042	9.1056	0.97209	2219
-0.35978	24.083	24.084	-0.16577	11.096	11.097	0.96643	11155
-3.6073	21.036	21.342	-1.6618	9.6908	9.8317	0.97236	9818
7.4053	25.138	26.192	3.2396	10.997	11.458	0.96112	856
-1.2546	22.046	22.081	-0.61213	10.756	10.773	0.97633	11148
-6.2106	17.165	18.253	-3.059	8.4546	8.9903	0.9796	5751
0.73326	18.633	18.647	0.33931	8.6223	8.6286	0.98632	12639

Preprints.org (www.preprints.org) | NOT PEER-REVIEWED | Posted: 4 July 2025 doi:10.20944/preprints202507.0386.v1

-2.0976	22.591	22.685	-0.85622	9.2214	9.2598	0.96951	3593
-2.2509	19.567	19.695	-1.0777	9.3678	9.4291	0.9794	9172
-0.20512	20.211	20.207	-0.087581	8.6298	8.6277	0.97007	1735
8.4614	17.614	19.54	4.3119	8.976	9.9575	0.9845	8217
1.0203	20.95	20.974	0.43742	8.9816	8.9917	0.97706	8037
1.9711	19.681	19.779	0.87726	8.7591	8.8025	0.98459	10238
-0.31496	23.435	23.434	-0.12177	9.0602	9.0602	0.97553	5389
-10.025	22.584	24.708	-4.2158	9.4968	10.39	0.9753	11163
-7.7282	25.605	26.741	-3.0347	10.054	10.5	0.94724	2568
-0.40962	24.71	24.712	-0.20687	12.479	12.48	0.97087	8537
-5.3007	23.663	24.248	-2.2613	10.095	10.344	0.97579	10506

Table C3. April, before removing outliers.

bias	stdev	rmserr	pbias	pstdev	prmserr	corr	numData
6.3927	32.54	33.161	2.0463	10.416	10.615	0.97869	13803
10.549	33.554	35.165	3.5387	11.256	11.796	0.9779	1906
8.7018	35.279	36.333	2.3276	9.4366	9.7186	0.97124	5346
5.2881	35.438	35.828	1.4071	9.4299	9.5336	0.98048	6976
-7.1726	36.432	37.129	-2.0231	10.276	10.472	0.98021	7656
-9.2121	33.955	35.179	-2.7715	10.215	10.584	0.97916	5023
-2.2479	29.31	29.394	-0.81003	10.562	10.592	0.98207	8921
4.1096	42.149	42.345	1.3431	13.776	13.839	0.95446	4816
-1.0489	37.602	37.612	-0.27951	10.02	10.023	0.9681	4669
6.0913	31.8	32.376	1.9959	10.42	10.609	0.97021	7534
14.012	33.614	36.405	5.343	12.817	13.881	0.95442	1186
12.612	29.678	32.245	4.4593	10.493	11.401	0.98153	7358
10.648	33.167	34.832	4.0319	12.558	13.189	0.96645	6445
14.713	29.905	33.327	5.0249	10.214	11.382	0.97588	7823
12.055	42.911	44.566	4.1201	14.666	15.232	0.93814	3647
10.795	36.486	38.047	2.879	9.731	10.147	0.97819	7805
9.1791	43.425	44.374	2.3281	11.014	11.255	0.97056	1999
8.8867	35.077	36.182	3.101	12.24	12.626	0.96343	5620
4.3037	28.102	28.428	1.6294	10.64	10.763	0.97121	7122
3.4387	20.621	20.891	1.7495	10.491	10.629	0.91169	719
9.2589	28.242	29.719	3.2688	9.9707	10.492	0.97567	7072
9.2641	32.509	33.8	3.8185	13.399	13.931	0.93371	5002
9.8469	37.58	38.846	2.8431	10.85	11.216	0.97455	7916
14.012	37.974	40.47	4.1579	11.268	12.009	0.97914	2999
2.7628	34.025	34.135	0.98996	12.192	12.231	0.97989	6002

Preprints.org (www.preprints.org) | NOT PEER-REVIEWED | Posted: 4 July 2025 doi:10.20944/preprints202507.0386.v1

3.7853	30.076	30.312	1.3343	10.602	10.685	0.98208	9373
0.66747	43.915	43.902	0.17523	11.529	11.526	0.95689	1238
5.2542	30.074	30.528	1.9433	11.123	11.291	0.98726	9744
-4.8184	33.678	34.019	-1.7026	11.9	12.021	0.97178	6646
6.4544	29.791	30.48	2.1917	10.116	10.35	0.97196	7348
2.8646	36.358	36.466	1.094	13.885	13.926	0.93823	3671
9.4512	34.751	36.011	3.0855	11.345	11.756	0.97421	7699
4.8481	36.47	36.782	1.9396	14.591	14.716	0.94603	2056
9.6587	30.278	31.779	3.7656	11.804	12.389	0.9691	5380
8.2933	36.907	37.825	2.6168	11.645	11.935	0.97417	6824
-11.632	48.193	49.547	-4.0388	16.733	17.203	0.91001	768
12.053	24.804	27.576	5.5133	11.346	12.614	0.94872	7105
5.0914	25.303	25.808	2.3969	11.912	12.15	0.90191	5158
10.944	24.307	26.656	4.71	10.461	11.472	0.95212	7544

Table C4. April, after removing outliers.

bias	stdev	rmserr	pbias	pstdev	prmserr	corr	numData
5.7429	30.536	31.07	1.8459	9.8147	9.9864	0.98122	13663
9.4321	30.652	32.062	3.2006	10.401	10.88	0.98105	1876
8.3125	33.613	34.622	2.2284	9.011	9.2816	0.97386	5309
5.3388	33.843	34.259	1.424	9.0266	9.1376	0.98218	6925
-5.4702	31.327	31.799	-1.5565	8.9142	9.0485	0.98525	7483
-8.0037	29.744	30.799	-2.4374	9.0582	9.3795	0.98324	4915
-1.0365	26.137	26.156	-0.37776	9.5258	9.5327	0.98501	8777
1.5724	34.7	34.732	0.51883	11.45	11.46	0.96922	4728
-0.91641	36.947	36.954	-0.24419	9.8448	9.8468	0.96928	4652
5.6348	29.836	30.361	1.8559	9.8268	9.9999	0.97349	7457
12.261	30.623	32.974	4.7278	11.808	12.715	0.9614	1164
12.129	27.753	30.286	4.3135	9.8697	10.771	0.98378	7282
8.7449	27.586	28.937	3.3768	10.652	11.174	0.97409	6314
14.089	27.333	30.749	4.848	9.405	10.58	0.97953	7710
9.1851	36.221	37.362	3.1936	12.594	12.991	0.95232	3572
10.013	34.207	35.641	2.6841	9.1692	9.5534	0.98069	7718
9.0734	41.881	42.842	2.3042	10.636	10.88	0.97259	1986
7.9169	30.833	31.831	2.7927	10.877	11.229	0.97096	5537
4.1334	26.627	26.944	1.5723	10.129	10.249	0.97384	7062
2.8696	16.602	16.837	1.4796	8.5601	8.681	0.93256	702
9.218	26.644	28.192	3.268	9.4459	9.9946	0.97821	7009
8.2833	28.202	29.39	3.4669	11.804	12.301	0.9432	4916

8.5062	33.941	34.988	2.4763	9.8805	10.185	0.97878	7814
13.531	36.142	38.586	4.034	10.775	11.503	0.98109	2971
3.0375	31.887	32.029	1.0955	11.501	11.552	0.98224	5943
3.6122	28.815	29.039	1.2802	10.212	10.292	0.98343	9306
1.1295	41.378	41.377	0.29675	10.872	10.871	0.96155	1227
5.8719	27.047	27.675	2.1909	10.092	10.326	0.98962	9618
-4.3313	31.925	32.215	-1.5344	11.31	11.413	0.97462	6589
6.0352	28.206	28.842	2.0615	9.6343	9.8518	0.97446	7284
2.6655	33.312	33.414	1.0255	12.816	12.856	0.94687	3623
8.7521	31.852	33.031	2.8916	10.524	10.913	0.97745	7600
4.0008	33.008	33.242	1.6157	13.33	13.425	0.95499	2026
9.6682	27.666	29.305	3.7885	10.841	11.483	0.97387	5324
7.6656	34.233	35.078	2.4391	10.893	11.162	0.97713	6749
-11.81	44.588	46.097	-4.1109	15.521	16.046	0.92294	760
11.907	22.435	25.398	5.5014	10.366	11.735	0.95468	7013
5.9755	22.021	22.816	2.8328	10.439	10.816	0.919	5068
10.655	21.083	23.621	4.6407	9.1826	10.288	0.95974	7413

Table C5 . July, before removing outliers.

bias	stdev	rmserr	pbias	pstdev	prmserr	corr	numData
20.694	26.243	33.42	10.155	12.878	16.4	0.90539	13375
17.396	24.854	30.33	9.0184	12.885	15.724	0.81099	1450
17.382	19.077	25.808	9.3403	10.251	13.868	0.94612	6854
17.248	38.868	42.521	7.0655	15.922	17.418	0.94271	6318
17.529	36.218	40.235	6.443	13.312	14.789	0.96597	7337
17.207	41.83	45.226	6.8164	16.57	17.916	0.9485	4223
16.589	41.72	44.895	6.8884	17.323	18.642	0.90333	7862
23.884	32.594	40.405	10.976	14.979	18.568	0.81538	3572
19.274	35.886	40.732	8.0807	15.045	17.077	0.91874	5104
18.971	28.491	34.228	8.4596	12.705	15.263	0.93202	7147
22.126	19.027	29.174	11.552	9.9338	15.232	0.8025	781
20.068	30.156	36.221	9.332	14.023	16.844	0.89747	7288
14.39	46.41	48.586	6.1757	19.917	20.851	0.89749	5674
21.455	35.36	41.358	8.1797	13.481	15.768	0.97334	8574
19.231	29.835	35.491	8.263	12.819	15.25	0.95823	2982
15.832	32.787	36.407	7.1771	14.864	16.505	0.91656	8194
36.126	38.139	52.524	16.093	16.989	23.397	0.8766	1460
19.98	23.786	31.063	9.5173	11.33	14.796	0.9216	6547
25.967	31.113	40.523	11.63	13.935	18.149	0.9173	6748
17.488	26.36	31.632	8.1182	12.237	14.684	0.93755	7575

doi:10.20944/preprints202507.0386.v1

21.096	45.586	50.226	8.9341	19.305	21.27	0.92596	4002
16.241	35.764	39.277	7.4357	16.374	17.983	0.94511	9544
17.692	35.198	39.386	6.9747	13.876	15.527	0.95725	1913
22.353	26.665	34.793	10.743	12.815	16.721	0.95804	5637
20.527	30.693	36.923	8.8063	13.168	15.841	0.96823	7738
18.071	18.083	25.556	9.2799	9.2858	13.124	0.85266	748
21.258	23.13	31.414	10.283	11.188	15.195	0.90377	7194
16.486	34.036	37.815	7.6338	15.76	17.51	0.90779	5015
17.992	33.435	37.967	7.9986	14.864	16.879	0.96283	8741
14.22	42.866	45.156	6.5271	19.675	20.727	0.8926	3123
17.346	31.992	36.39	7.7389	14.273	16.235	0.9334	8265
18.95	34.228	39.122	9.914	17.907	20.467	0.93652	8263
15.842	41.009	43.959	6.4923	16.806	18.015	0.93568	6021
16.998	30.122	34.586	8.2244	14.574	16.734	0.96407	9760
10.441	38.427	39.816	4.6305	17.042	17.658	0.90742	4045
14.949	42.506	45.056	6.3811	18.145	19.233	0.94592	8930
16.466	41.38	44.526	7.1613	17.996	19.365	0.91668	2006
16.462	31.506	35.546	9.169	17.548	19.798	0.96213	8657

Table C6. July, after removing outliers.

bias	stdev	rmserr	pbias	pstdev	prmserr	corr	numData
20.162	17.694	26.825	10.058	8.827	13.382	0.94183	13157
15.538	19.346	24.808	8.2128	10.225	13.112	0.83343	1406
16.147	15.84	22.619	8.8078	8.64	12.338	0.95758	6680
16.284	29.022	33.276	6.8307	12.174	13.958	0.96273	6187
15.951	30.023	33.995	6.0162	11.324	12.822	0.97314	7198
17.101	35.894	39.756	6.8684	14.416	15.967	0.96034	4149
15.806	31.638	35.365	6.704	13.419	14.999	0.92942	7693
22.038	27.934	35.578	10.271	13.018	16.581	0.82959	3507
17.824	28.223	33.378	7.6048	12.042	14.241	0.94312	5001
18.692	24.104	30.501	8.4616	10.912	13.807	0.93977	7023
19.399	15.046	24.544	10.334	8.0148	13.074	0.79435	740
18.939	23.247	29.984	8.9751	11.016	14.209	0.9253	7123
12.903	37.593	39.743	5.6825	16.556	17.502	0.92159	5545
19.203	28.49	34.356	7.5994	11.275	13.596	0.97827	8320
17.535	24.869	30.426	7.6788	10.891	13.324	0.96665	2925
16.124	26.863	31.329	7.3912	12.314	14.361	0.93679	8044
35.314	36.139	50.519	15.873	16.244	22.708	0.88008	1444
19.155	20.585	28.118	9.2091	9.8966	13.518	0.93346	6448

Preprints.org (www.preprints.org) | NOT PEER-REVIEWED | Posted: 4 July 2025 doi:10.20944/preprints202507.0386.v1

24.749	28.397	37.667	11.234	12.89	17.098	0.92199	6615
16.299	22.253	27.582	7.7269	10.549	13.076	0.93617	7441
18.47	34.259	38.917	8.1598	15.135	17.193	0.93916	3884
16.353	27.256	31.784	7.6126	12.688	14.796	0.96403	9391
17.826	28.326	33.462	7.1407	11.347	13.404	0.96973	1869
20.685	20.199	28.91	10.251	10.01	14.327	0.96591	5501
19.125	24.261	30.892	8.5313	10.823	13.78	0.97116	7559
17.864	14.455	22.974	9.2828	7.5113	11.938	0.87414	728
20.179	19.641	28.158	9.8831	9.6196	13.791	0.91472	7051
15.58	25.327	29.733	7.4048	12.038	14.132	0.93112	4898
15.246	26.609	30.666	7.119	12.425	14.319	0.9637	8480
12.084	34.548	36.595	5.7036	16.307	17.273	0.91312	3047
16.784	26.36	31.249	7.6477	12.011	14.238	0.94342	8107
16.226	22.013	27.345	8.822	11.968	14.868	0.95987	8084
14.094	31.501	34.508	5.9873	13.382	14.66	0.94835	5862
15.628	23.58	28.288	7.7619	11.711	14.049	0.97361	9576
10.106	33.318	34.813	4.5379	14.96	15.631	0.92451	3982
12.974	33.189	35.633	5.7596	14.733	15.818	0.95523	8686
15.296	33.682	36.985	6.7889	14.949	16.415	0.93892	1963
13.767	19.637	23.981	8.169	11.652	14.23	0.97366	8420

doi:10.20944/preprints202507.0386.v1

Appendix D

Results for January, April, and July using all available observations

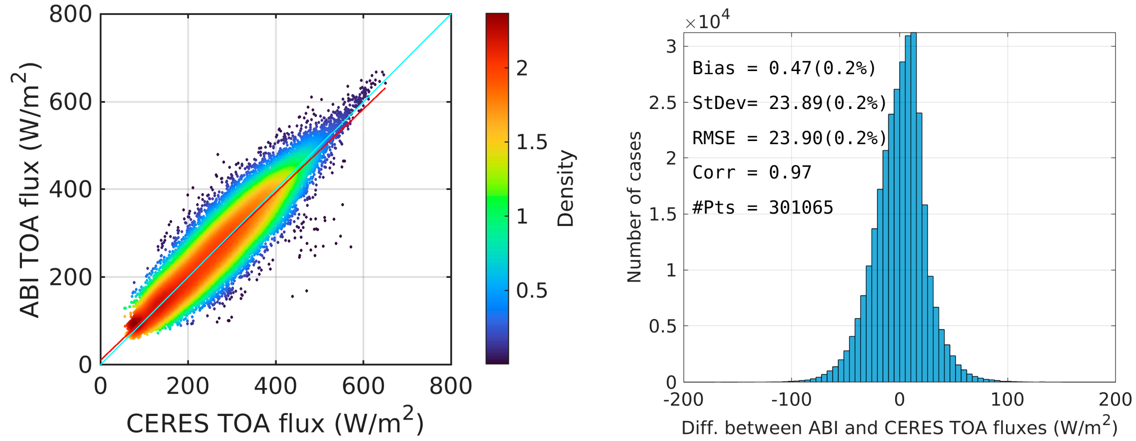

Figure D1. ABI TOA flux compared to CERES TOA flux for January 2023.

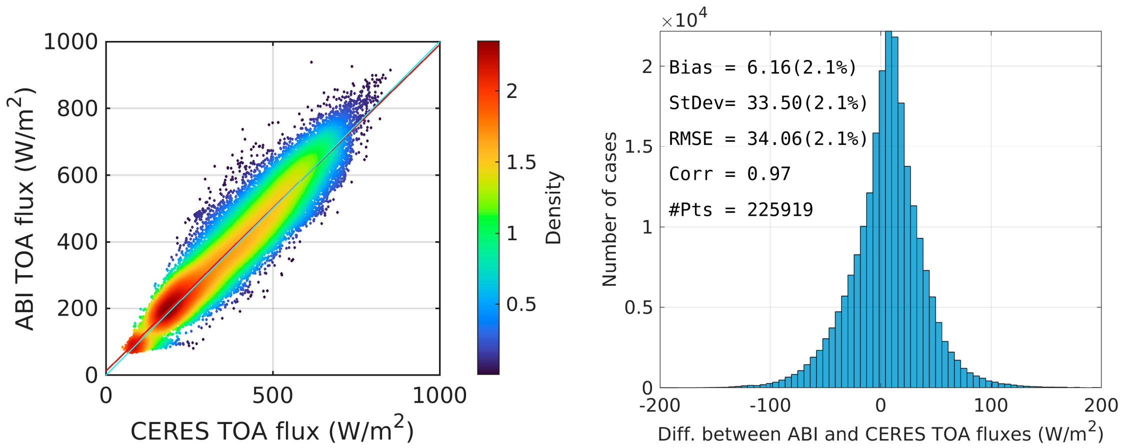

Figure D2. ABI TOA flux compared to CERES TOA flux for April 2023.

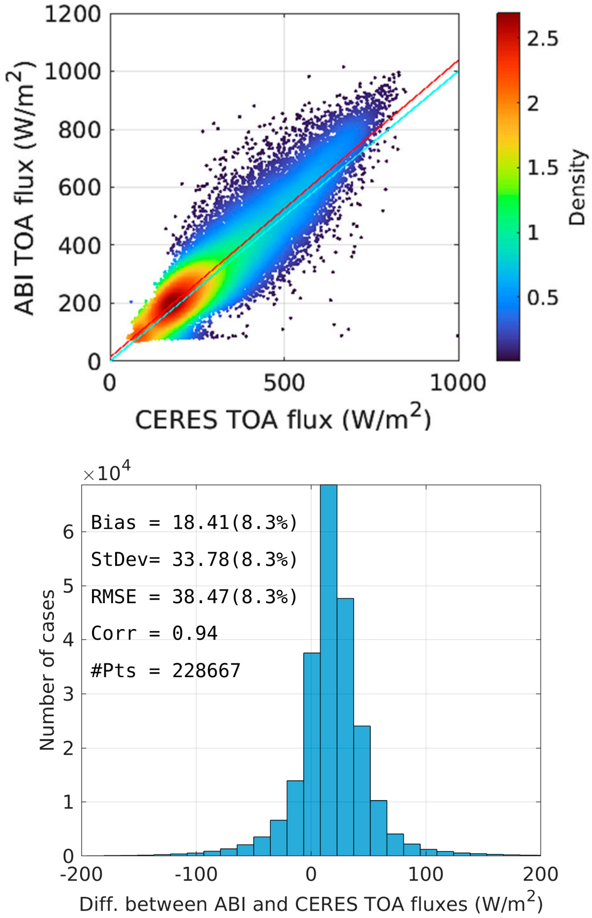

Figure D3. ABI TOA flux compared to CERES TOA flux for July 2023.

References

1. Laszlo, I., Liu, H., Kim, H.-Y and Pinker R. T. (2018). GOES-R Advanced Baseline Imager (ABI) Algorithm Theoretical Basis Document (ATBD) for Downward Shortwave Radiation (Surface), and Reflected Shortwave Radiation (TOA), version 3.1. Available at https://www.goes-r.gov/resources/docs.html
2. Laszlo, I., Liu, H., Kim, H.-Y and Pinker R. T (2020). Shortwave Radiation from ABI on the GOES-R Series, in *The GOES-R Series*, edited by S. J. Goodman, T. J. Schmit, J. Daniels and R. J. Redmon, pp. 179-191, Elsevier, doi: https://doi.org/10.1016/B978-0-12-814327-8.00015-9.
3. Pinker, R. T., Ma, Y., Chen, W., Laszlo, I., Liu, H., Kim H.-K., and Daniels, J. (2022). Top of the Atmosphere Reflected Shortwave Radiative Fluxes from GOES R. *Atmos. Meas. Tech*., 15, 5077–5094.
4. Berk et al., 1998. MODTRAN Cloud and Multiple Scattering Upgrades with Application to AVIRIS. Berk et al. (1998). MODTRAN Cloud and Multiple Scattering Upgrades with Application to AVIRIS. *Remote Sensing of Environment*, 65 (3), 367-375.
5. Hansen, M. C., Defries, R. S., Townshend, J. R. G., and Sohlberg, R. (2010). Global land cover classification at 1km spatial resolution using a classification tree approach, *Int. J. Remote Sens*., 21, 1331–1364, https://doi.org/10.1080/014311600210209.
6. Loeb, N. G., Smith, N. M., Kato, S., Miller, W. F., Gupta, S. K., Minnis, P., and Wielicki, B. A. (2003). Angular Distribution Models for Top-of Atmosphere Radiative Flux Estimation from the Mission Satellite, Part I: Methodology. *J. Appl. Meteorol*., 42, 240–265.
7. Niu, X. and Pinker, R. T. (2011). Revisiting satellite radiative flux computations at the top of the atmosphere, *International Journal of Remote Sensing*, DOI:10.1080/01431161.2011.571298
8. Loveland, T. R., Reed, B. C., Brown, J. F., Ohlen, D. O., Zhu, Z., Yang, L., and Merchant, J. W. (2010). Development of a global land cover characteristics database and IGBP DISCover from 1 km AVHRR data, *Int. J. Remote Sens*., 21, 1303–1330.

 doi:10.20944/preprints202507.0386.v1

9. Su, W., Corbett, J., Eitzen, Z., and Liang, L. (2015). Next-generation angular distribution models for top-of-atmosphere radiative flux calculation from CERES instruments: methodology, 2015. *Atmos. Meas. Tech.*, 8, 611–632, https://doi.org/10.5194/amt-8-611-2015.
10. Su, W., Corbett, J., Eitzen, Z., and Liang, L. (2015). Next-generation angular distribution models for top-of-atmosphere radiative flux calculation from CERES instruments: validation, 2015. *Atmos. Meas. Tech.*, 8, 3297–3313, https://doi.org/10.5194/amt-8-3297-2015.